

Supplementary Material

S.1 Chapter 1

There is no supplement material for Chapter 1.

S.2 Chapter 2

Model Name	Ref-C2 (1960–2100) No of simulations used
ACCESSCCM	1*
CCSRNIES MIROC3.2	2*
CESM1 CAM4-chem	3
CESM1 WACCM	3
CHASER(MIROC-ESM)	1
CMAM	1*
CNRM-CM5-3	2*
EMAC	3*
GEOSCCM	1*
HadGEM3-ES	1
LMDz–REPROBUS	1 (L39)
MRI-ESM1r1	1
NIWA-UKCA	5
SOCOL	1*
ULAQCCM	3*
UMSLIMCAT	1*
Total	29

Table S2.1: CCM1-1 models and the number of REF-C2 simulations used in the calculation of the multi-model mean ozone anomaly time series and ozone profiles.

For the full list of models, model versions and key references please refer to *Morgenstern et al. (2017)*.

* Models using prescribed ocean, for details see Table S1 in the supplement of *Morgenstern et al. (2017)*.

S.3 Chapter 3

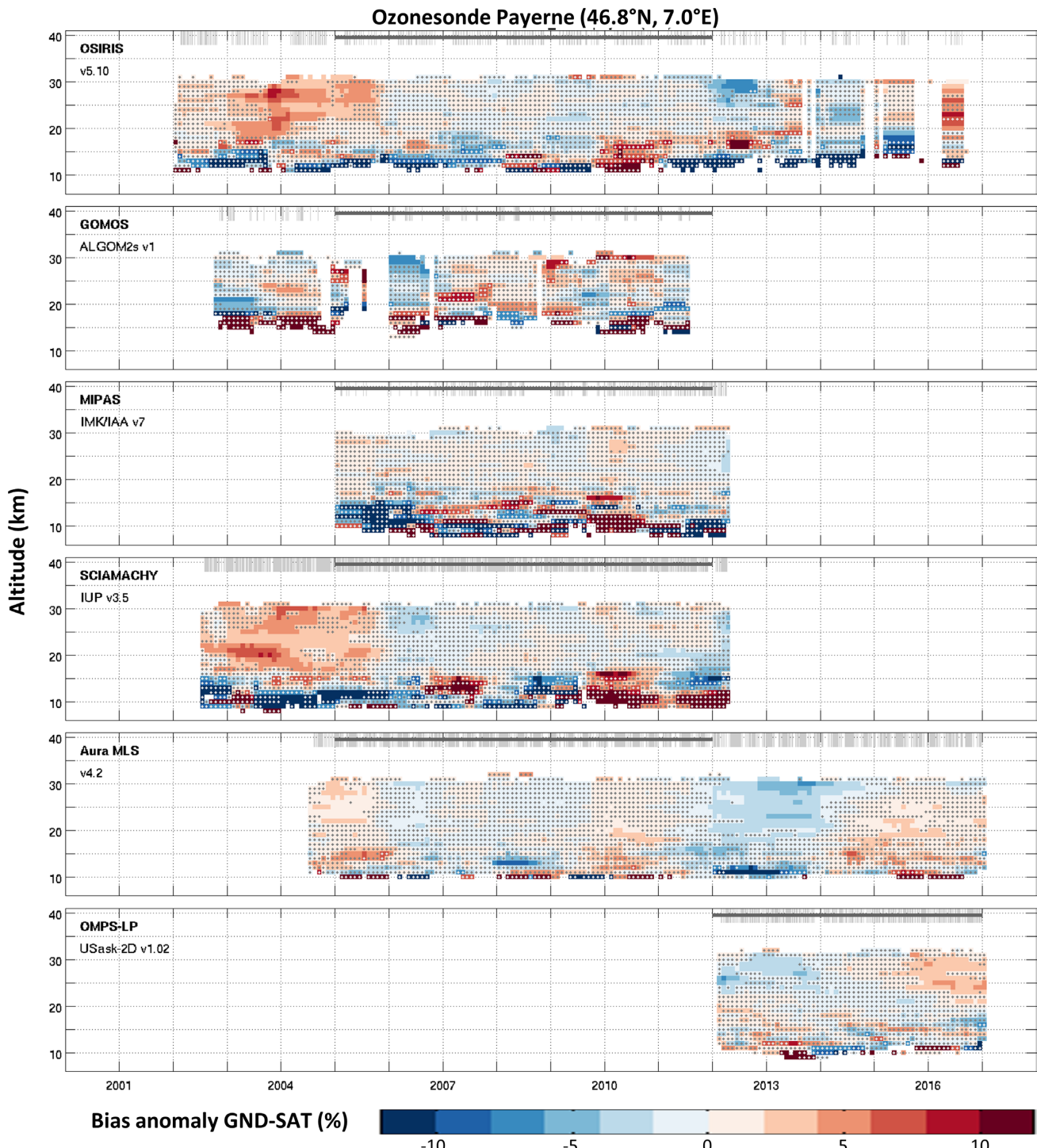


Figure S3.1: Smoothed anomaly time series (δ , see Equation 3.1) of the relative difference of Payerne ozonesonde and six satellite ozone profile data records (top to bottom). Red values indicate regions in which sonde measurements are biased more positive (or less negative) compared to satellite than their median value during the reference period. Stippled areas denote δ values that are not statistically different from zero at the 2-sigma level. A running average with a 12-month window was used to smooth the time series. Thin grey vertical lines show the sampling of the co-located profile data records; the grey horizontal lines indicate the reference period for each comparison. A selection of these panels was shown in **Figure 3.2**. Adapted from Hubert et al. (2019).

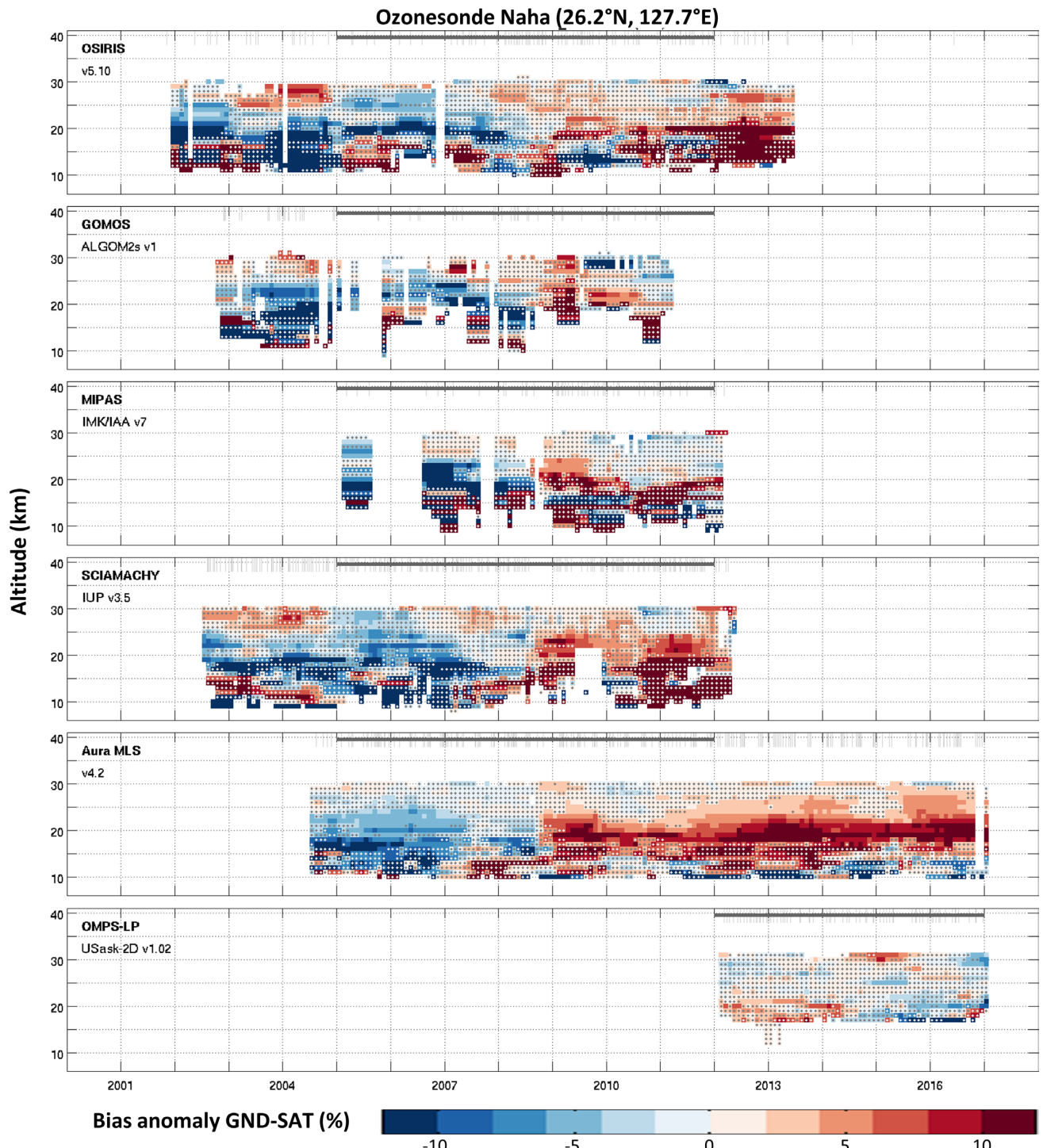


Figure S3.2: As **Figure S3.1**, but for the Naha ozonesonde. Stippled areas denote non-significant δ values. A selection of these panels was shown in **Figure 3.2**. Adapted from Hubert et al. (2019).

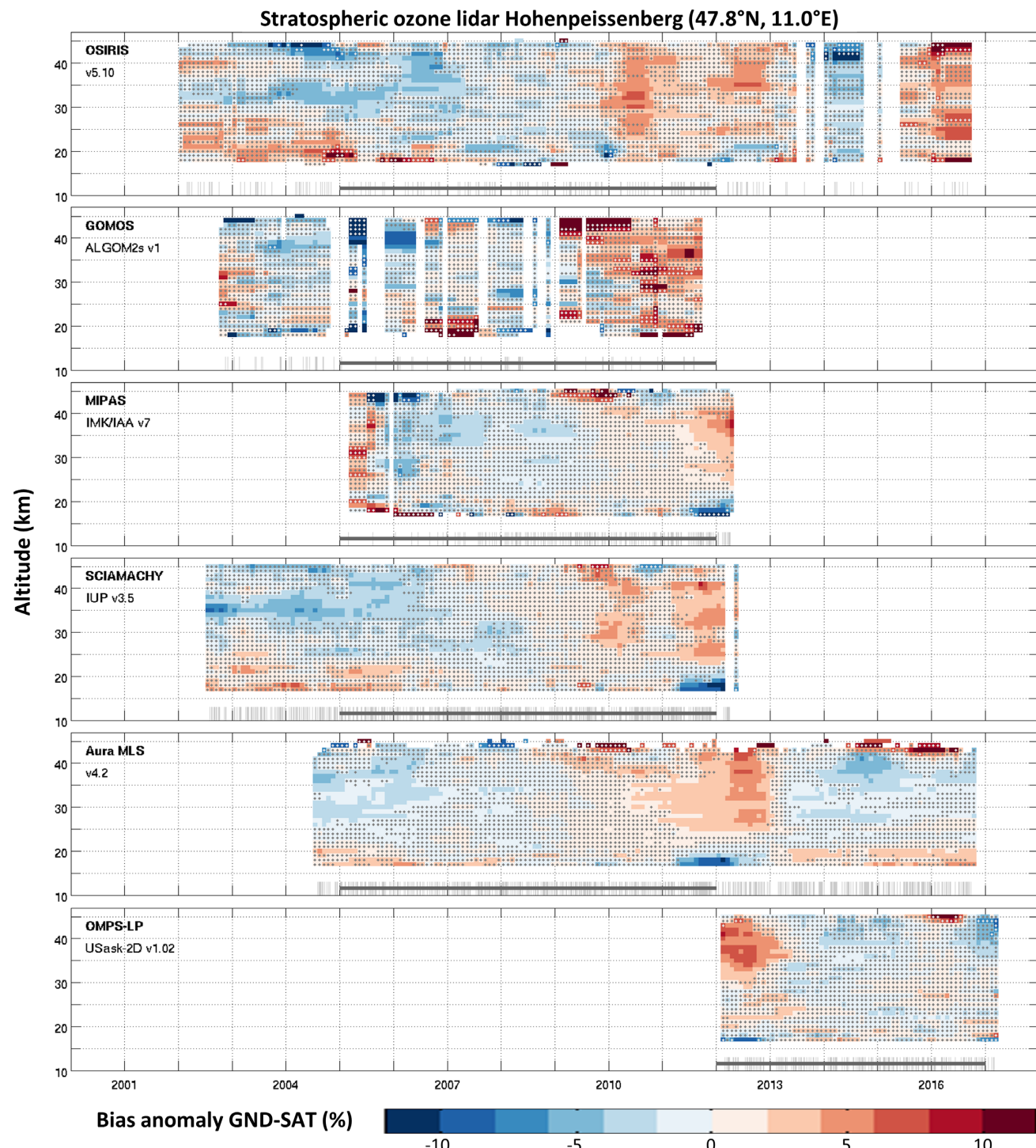


Figure S3.3: As **Figure S3.1**, but for the Hohenpeissenberg lidar. Stippled areas denote non-significant δ values. A selection of these panels was shown in **Figure 3.3**. Adapted from Hubert et al. (2019).

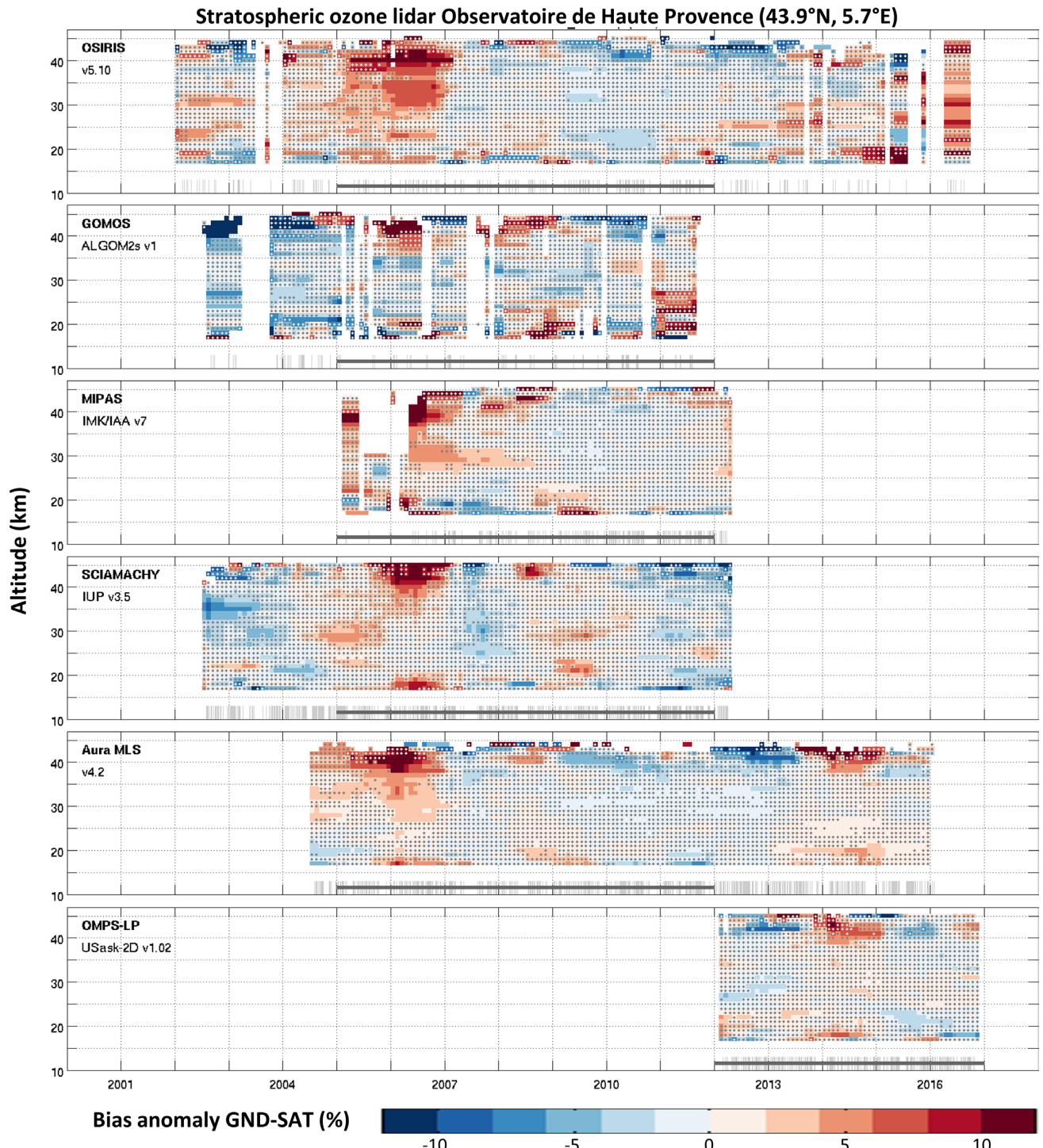


Figure S3.4: As **Figure S3.1**, but for the OHP lidar. Stippled areas denote non-significant δ values. A selection of these panels was shown in **Figure 3.3**. Adapted from Hubert et al. (2019).

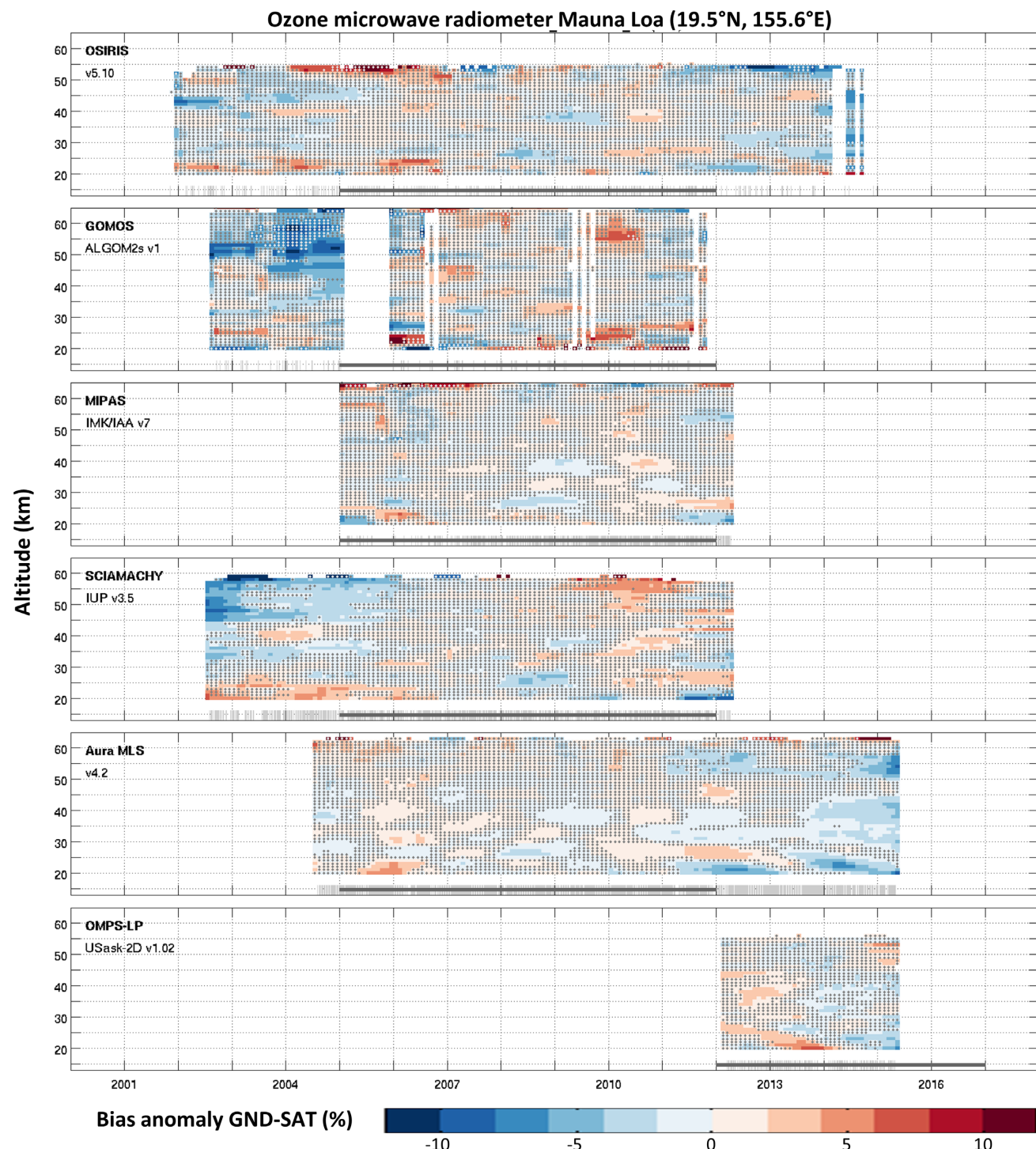


Figure S3.5: As **Figure S3.1**, but for the MLO radiometer. Stippled areas denote non-significant δ values. A selection of these panels was shown in **Figure 3.4**. Adapted from Hubert et al. (2019).

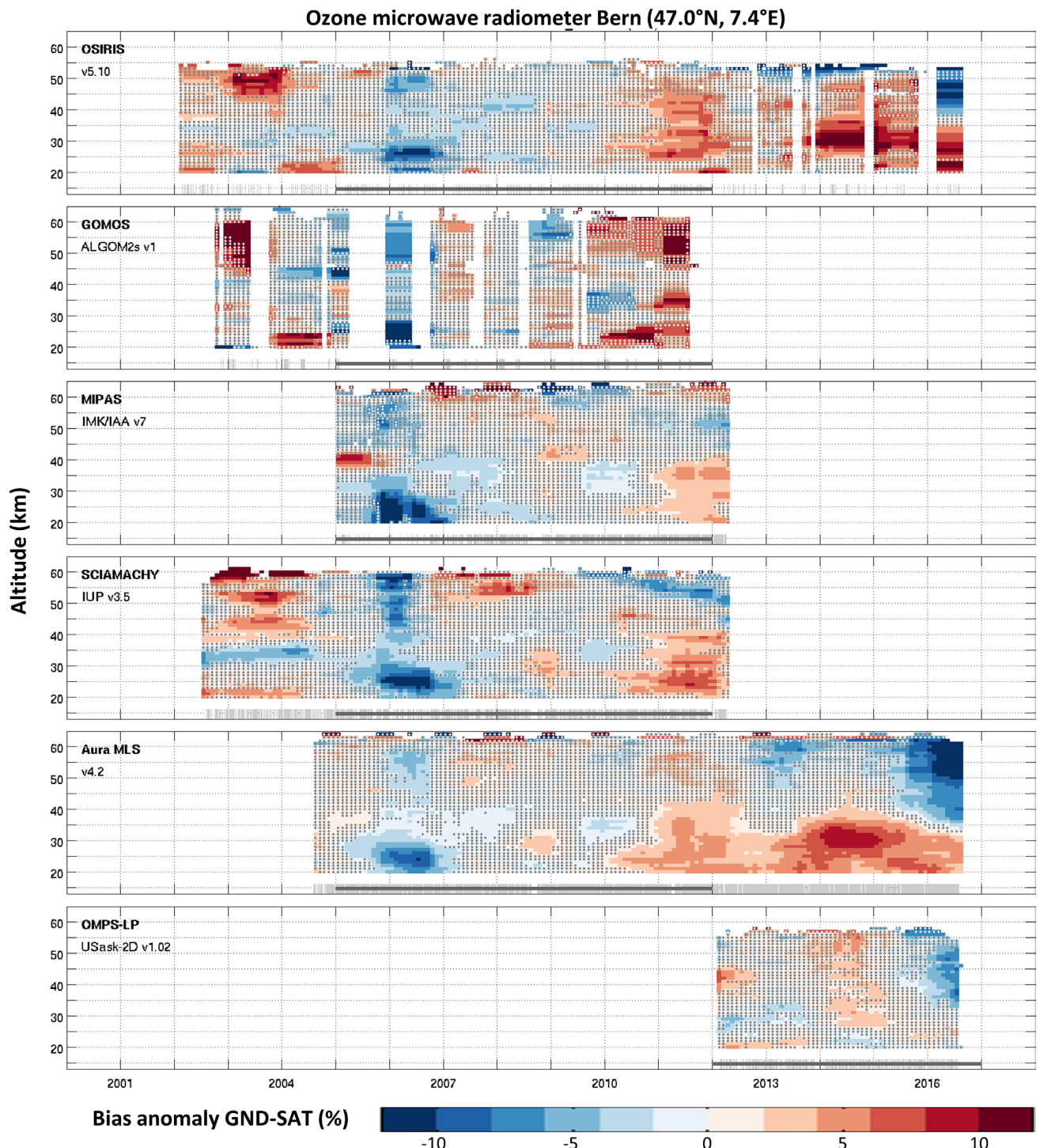


Figure S3.6: As **Figure S3.1**, but for the Bern radiometer. Stippled areas denote non-significant δ values. A selection of these panels was shown in **Figure 3.4**. Adapted from Hubert et al. (2019).

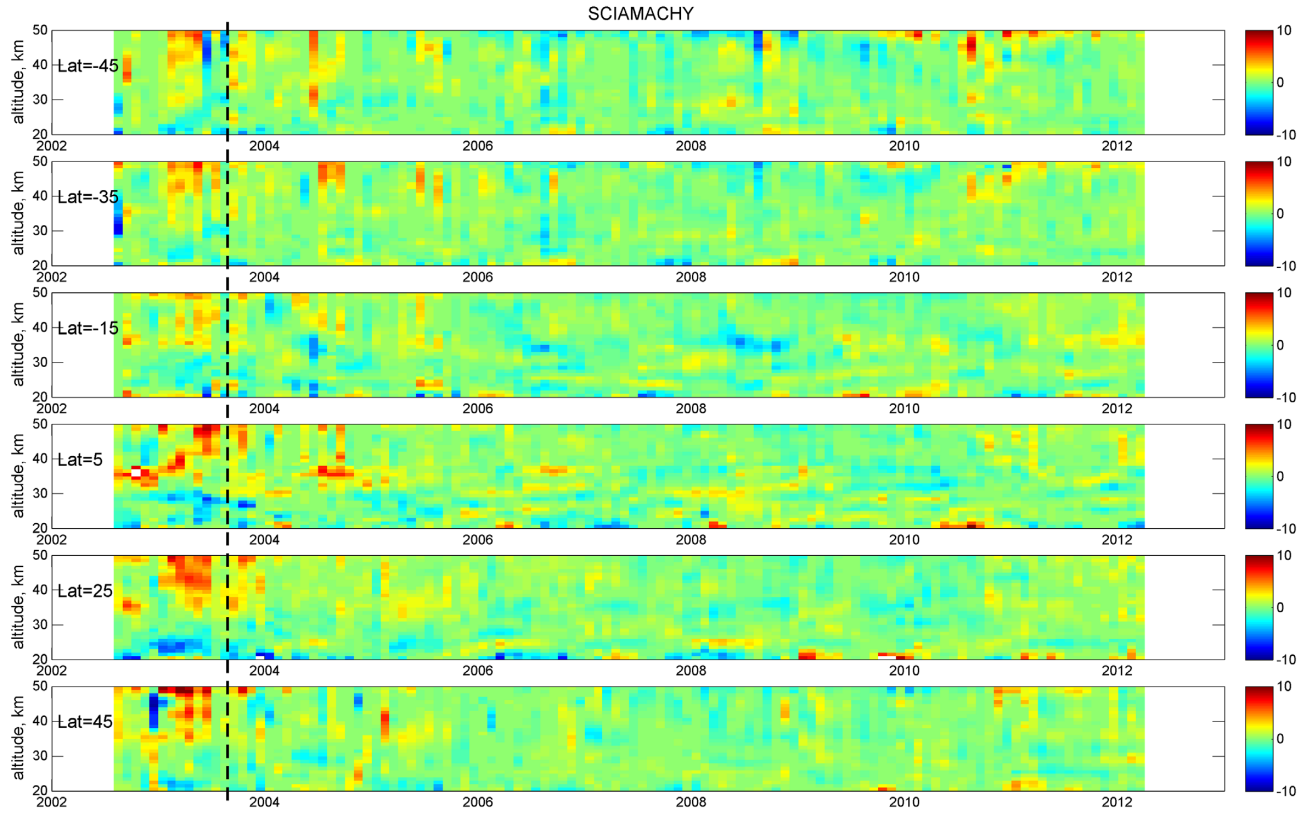


Figure S3.7: Deviations (in %, color) of SCIAMACHY deseasonalised anomalies from the median deseasonalised anomalies of SAGE II, GOMOS, MIPAS, SCIAMACHY, OSIRIS, ACE-FTS and OMPS. 10° latitude bands are indicated by their centres in the panels. The dashed line indicates the early part of the mission during which significant deviations from the median deseasonalised anomalies are observed. From Sofieva et al. (2017).

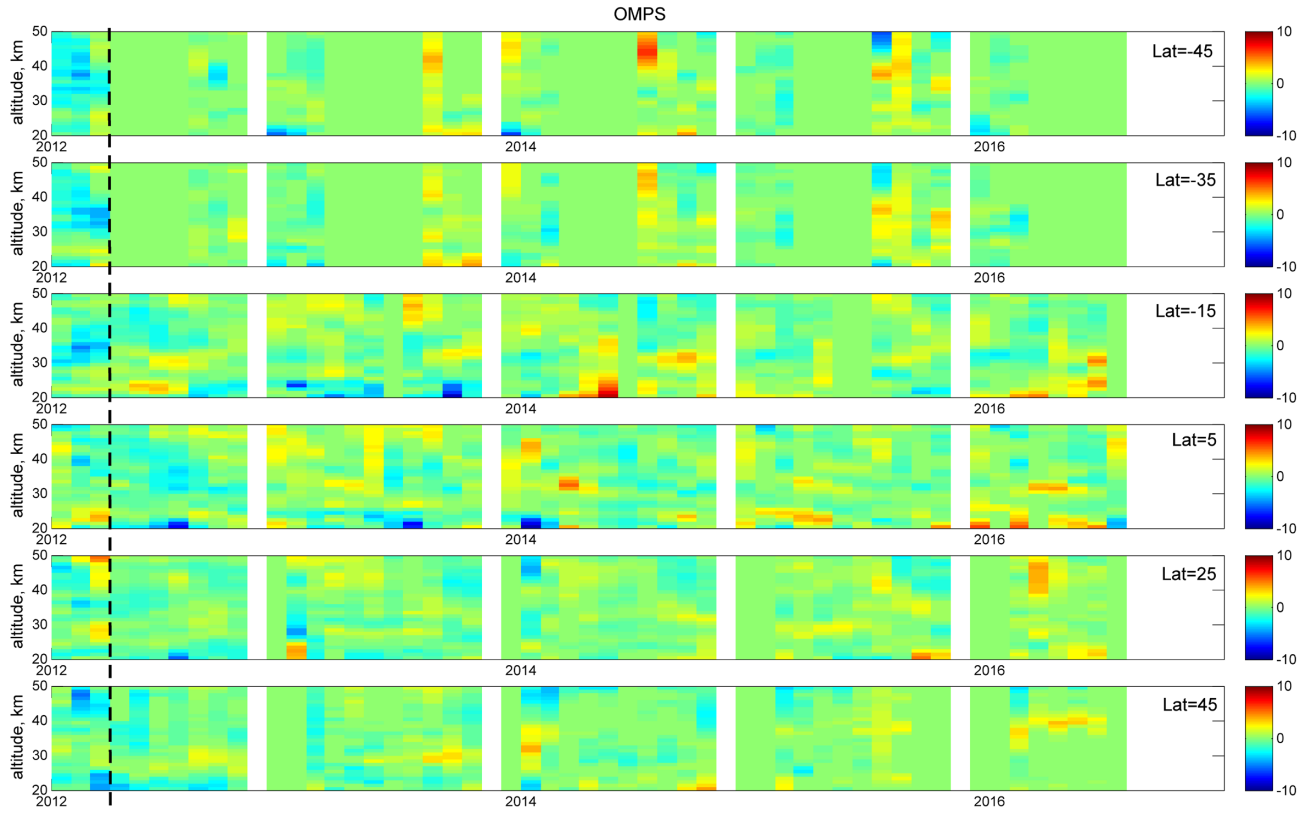


Figure S3.8: As Figure S3.7 but for the OMPS-LP deseasonalised anomalies. From Sofieva et al. (2017).

S.4 Chapter 4

S.4.1 DLM estimated ozone changes from the BASIC composites

The following supplementary information shows analyses of ozone composites merged using the BASIC algorithm (*Ball et al.*, 2017) that was applied to four sets of composites: BASIC_v2, BASIC v2_SG, BASIC v2_SBUV, and BASIC v2_nden. BASIC_v2 extends the four composites used in *Ball et al.* (2017): SWOOSH, GOZCARDS, SBUV-COH, and SBUV-MOD. BASIC v2_SG combines just GOZCARDS and SWOOSH since they are based on similar underlying instrument data (as presented in *Ball et al.* (2018)). BASIC v2_SBUV combines SBUV_COH and SBUV-MOD (see also *Ball et al.* (2018)). BASIC v2_nden combines SAGE II-OSIRIS-OMPS, SAGE II-MIPAS-OMPS, and SAGE II-CCI-OMPS (see *Chapter 3* of the Report). Version 1 of BASIC considered earlier versions of the datasets until 2012 (*Ball et al.*, 2017), while version 2 uses the updated composites presented in this Report and extended until 2016 (2015 for the BASIC v2_nden).

The analysis considers DLM (*Laine et al.*, 2014; *Ball et al.*, 2017, 2018) instead of MLR, and the regressors used are similar, though not identical, to those used in this Report and are also the regressors used for the analysis of *Ball et al.* (2017, 2018). The regressors include: A solar proxy (30 cm radio flux), a volcanic proxy (latitude-dependent SAD, based on *Thomason et al.*, 2018), two QBO proxies (30 hPa and 50 hPa wind fields as provided by the Freie University Berlin), and an ENSO proxy (Nino 3.4 HadSST). Seasonal cycle components, AR2 processes, and residuals are estimated together with these regressors as well as the non-linear background trend. This non-linear background trend replaces the use of ILT, PWLT, or EESC and does not require an assumption about inflection dates, only a prior assumption about the smoothness of the non-linear background changes being estimated, which is determined from the data itself (see *Laine et al.* (2014) for further details, and *Ball et al.* (2017) for minor changes to the DLM algorithm used here). Because the background changes are non-linear, quoting a % per decade trend is not appropriate, so we instead quote changes between the beginning and end of the period (**Figures S4.1, S4.2, and S4.3**), which is partly analogous to the decadal trends quoted elsewhere in the Report. **Figure S4.3** is rescaled to an approximately decadal change (by factors of 1.5 and 1.6 for the earlier and latter periods) to yield **Figure S4.4**, for comparison with other trends shown in this Report.

All figures show percentage ozone changes between January 1985 and December 1999 (upper rows) and January 2000 and December 2016 (2015 for BASIC v2_nden) in three latitudinal bands (60°S–35°S, 20°S–20°N, and

35°N–60°N). **Figure S4.1** provides estimates for VMR-based BASIC composites on pressure levels (v2, v2_SG, and v2_SBUV), while **Figure S4.2** provides results for BASIC v2_nden on altitude levels. **Figures S4.3 and S4.4** present all composites on approximately the same levels scaling number density on altitude levels to VMR on pressure levels, with the assumption that 16–48 km converts to approximately 100–1 hPa.

The following bullets are some brief comments on comparisons of the DLM-BASIC results here with those presented in *Chapter 5*, noting that in those figures the earlier period spans 1985 to 1996 (and not 1985 to 1999 as reported here):

- results between those presented here and those in *Section 5.3* are generally very similar; there is slightly lower significance (larger uncertainties) in the DLM results in the upper stratosphere in the post-2000 period;
- above 10 hPa most results agree well between DLM estimates using the BASIC merging algorithm and those following the procedures laid out in *Section 5.3*;
- SH changes in the earlier period in the DLM-BASIC results do not show large positive trend in the lower stratosphere, such that the number density and vmr estimates are similar in the DLM (**Figure S4.3**), and NH and SH trends are approximately symmetric from the DLM-BASIC analysis;
- in the earlier period, equatorial (20°S–20°N) DLM-BASIC estimated changes show different estimates for number density and VMR BASIC composites close to 100 hPa, while limb VMR and limb NDEN appear similar in *Section 5.3*; similarity near 100 hPa for the DLM-BASIC results (**Figures S4.3 and S4.4**) is also partly the case for the latter period (2000–2015/2016).
- significance exists in the DLM-BASIC results, but is slightly lower, around 3 hPa compared to *Section 5.3* (although the mean magnitude of the trend/change is similar (**Figure S4.4**));
- BASIC v2 (merging all VMR composites) shows a more ‘mean’ like profile of the two merged-pairs (BASIC v2_SG and BASIC v2_SBUV) in the upper stratosphere (above 10 hPa), but is in more agreement with one of the pairs in the altitude region below 10 hPa (**Figure S4.1**). This is likely because there is less evidence for problems (e.g., drifts and discontinuities) in the upper stratosphere so they end up being weighted more evenly, though the mean is not always half-way between trend results for the two merged pairs.

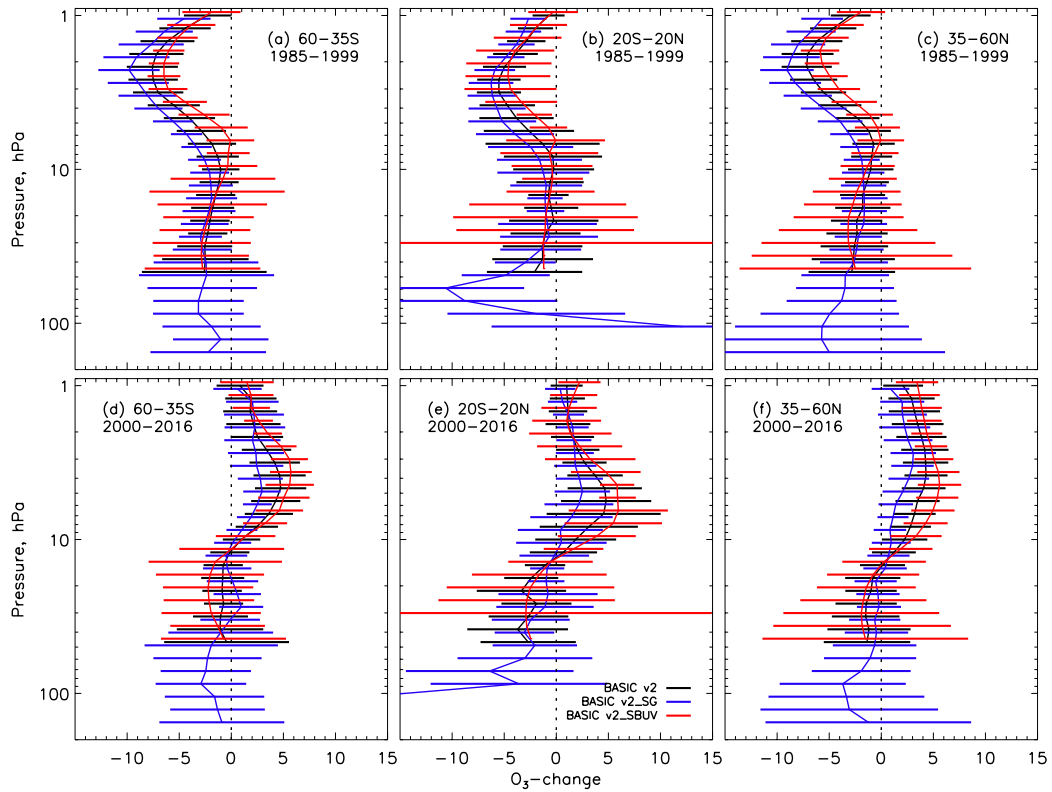


Figure S4.1: VMR-based profiles of ozone change (%) using DLM analysis for the three broad latitude bands (60°S – 35°S , 20°S – 20°N , and 35°N – 60°N) and two time periods (Jan 1985 to Dec 1999 and Jan 2000 and Dec 2015). Error bars are 2-sigma.

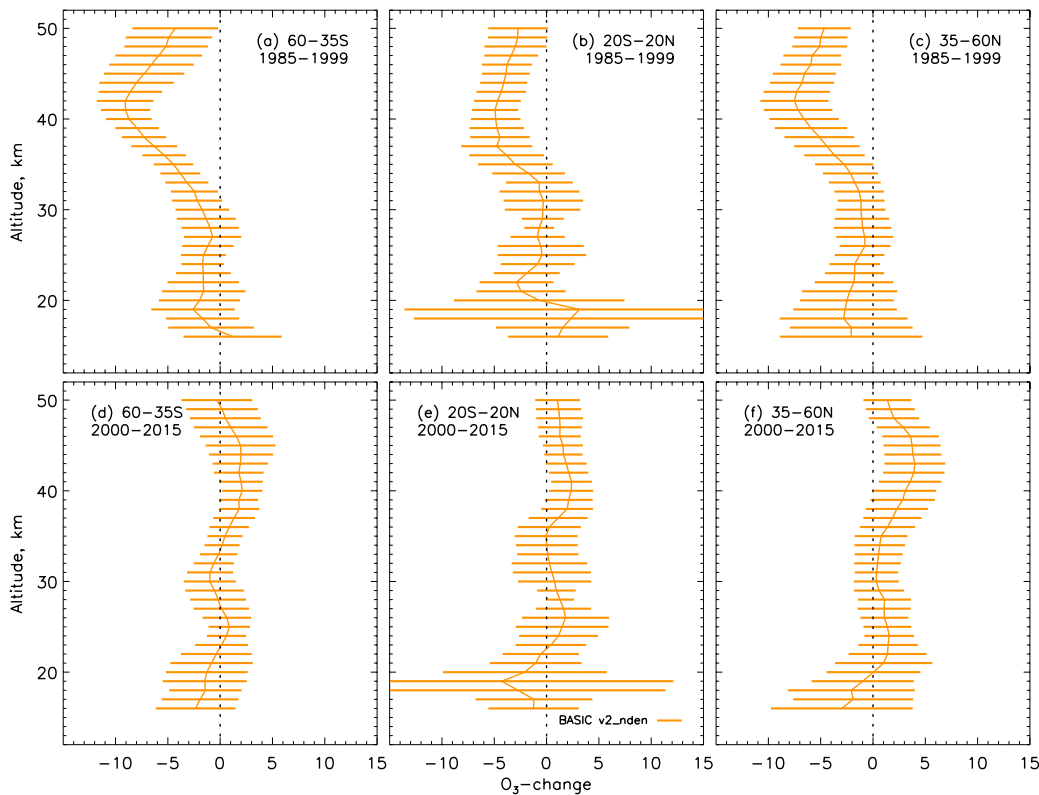


Figure S4.2: Number density-based profiles of ozone change (%) using DLM analysis for the three broad latitude bands (60°S – 35°S , 20°S – 20°N , and 35°N – 60°N) and two time periods (Jan 1985 to Dec 1999 and Jan 2000 and Dec 2015). Error bars are 2-sigma.

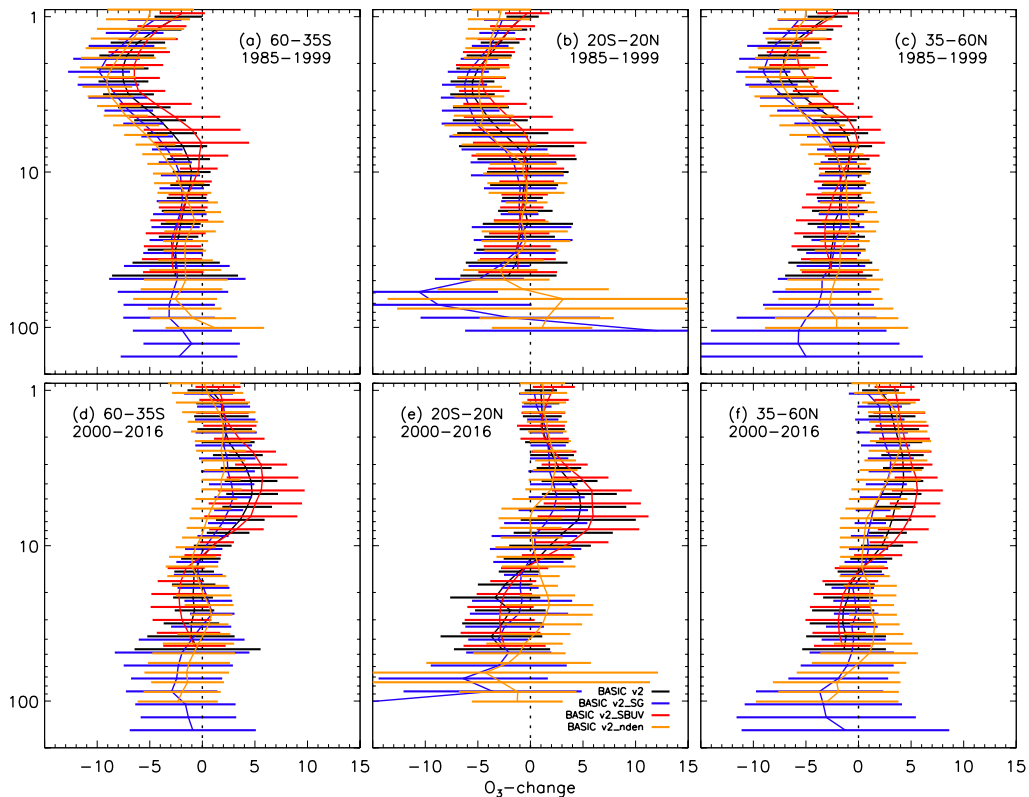


Figure S4.3: VMR-based and number density profiles of change in ozone (%) from DLM analysis for the three broad latitude bands (60°S – 35°S , 20°S – 20°N , and 35°N – 60°N) and two time periods (Jan 1985 to Dec 1999 and Jan 2000 and Dec 2015). Error bars are 2-sigma. Number density on altitude profiles are approximately scaled to pressure profiles with $100 \text{ hPa} \sim 16 \text{ km}$ and $1 \text{ hPa} \sim 48 \text{ km}$.

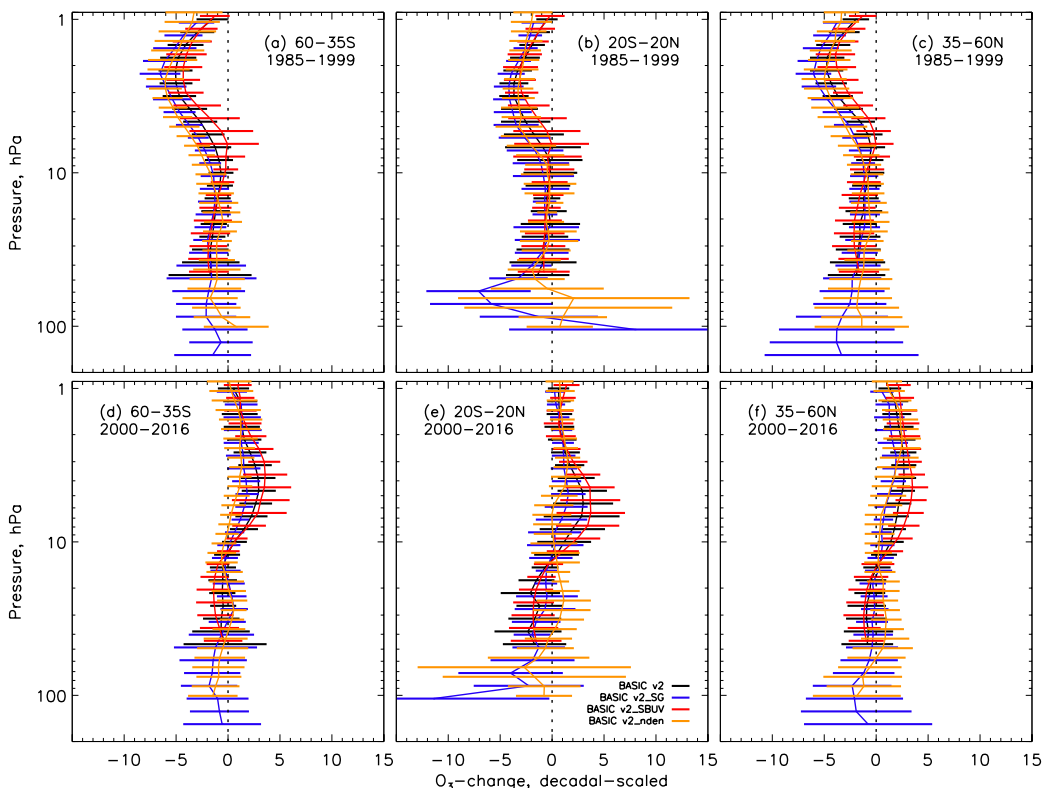


Figure S4.4: VMR-based profiles for change in ozone (scaled to % per decade) from DLM analysis, rescaled from Figure S4.3 for the three broad latitude bands (60°S – 35°S , 20°S – 20°N , and 35°N – 60°N) and two time periods (Jan 1985 to Dec 1999 and Jan 2000 and Dec 2015/2016). Error bars are 2-sigma.

S.5 Chapter 5

S.5.1 Appendix A: Supplementary figures

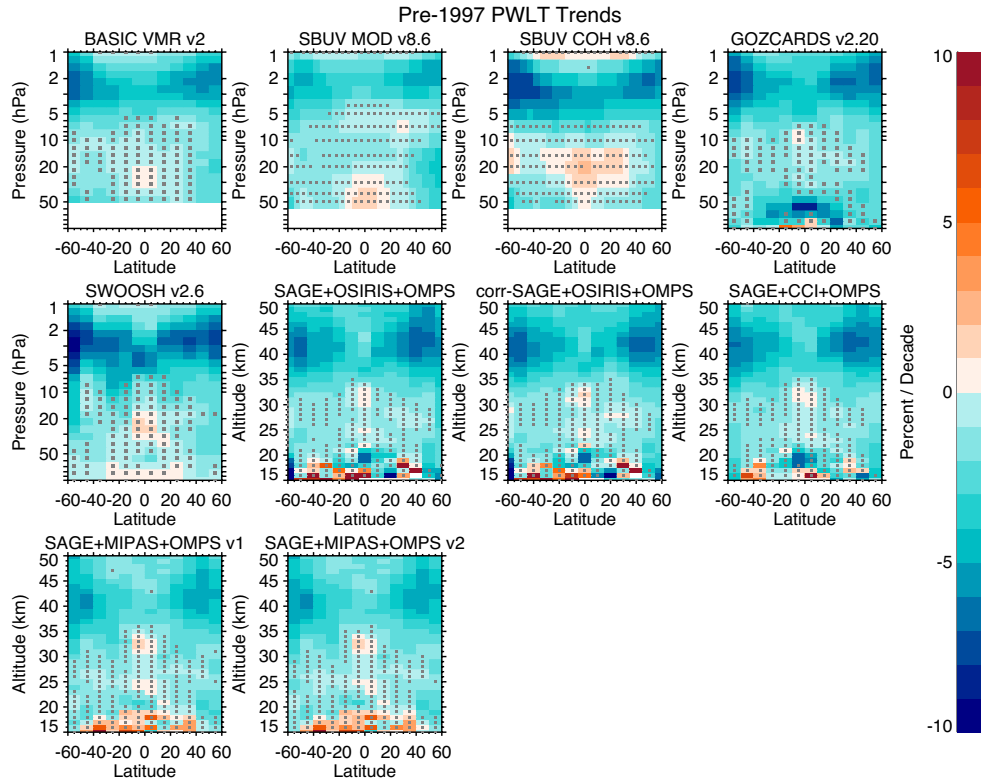


Figure S5.1: Derived trends in ozone in percent per decade for the pre-1997 period (Jan 1985 – Dec 1996) for each of the satellite data sets, using the PWLT trend proxy in a regression analysis. Grey stippling denotes results that are not significant at the 2-sigma level. Data are presented on their natural latitudinal grid and vertical coordinate.

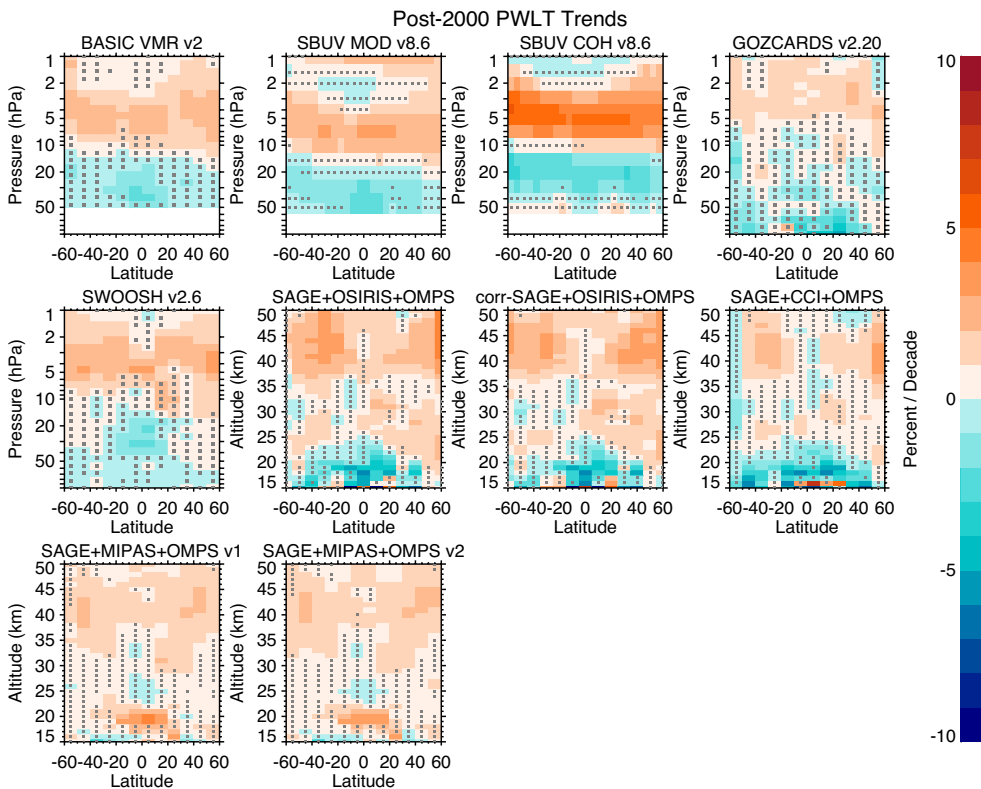


Figure S5.2: Derived trends in ozone in percent per decade for the post-2000 period (Jan 2000 – Dec 2016) for each of the satellite data sets, using the PWLT trend proxy in a regression analysis. Grey stippling denotes results that are not significant at the 2-sigma level. Data are presented on their natural latitudinal grid and vertical coordinate.

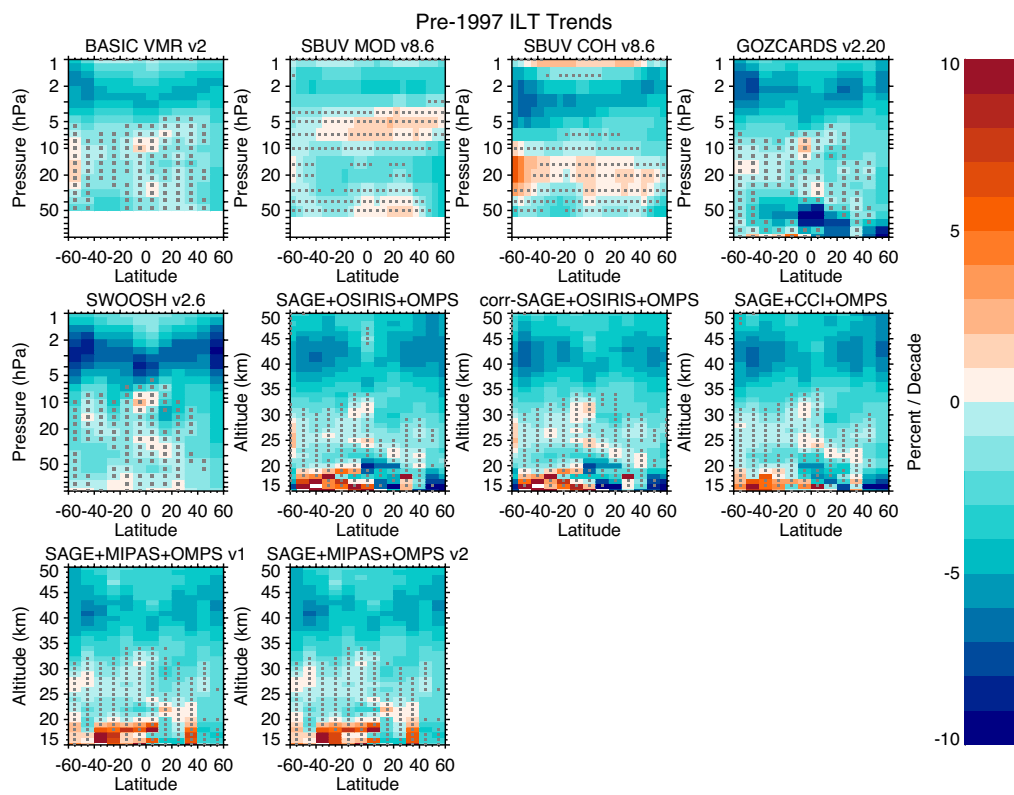


Figure S5.3: Derived trends in ozone in percent per decade for the pre-1997 period (Jan 1985 – Dec 1996) for each of the satellite data sets, using the ILT trend proxy in a regression analysis. Grey stippling denotes results that are not significant at the 2-sigma level. Data are presented on their natural latitudinal grid and vertical coordinate.

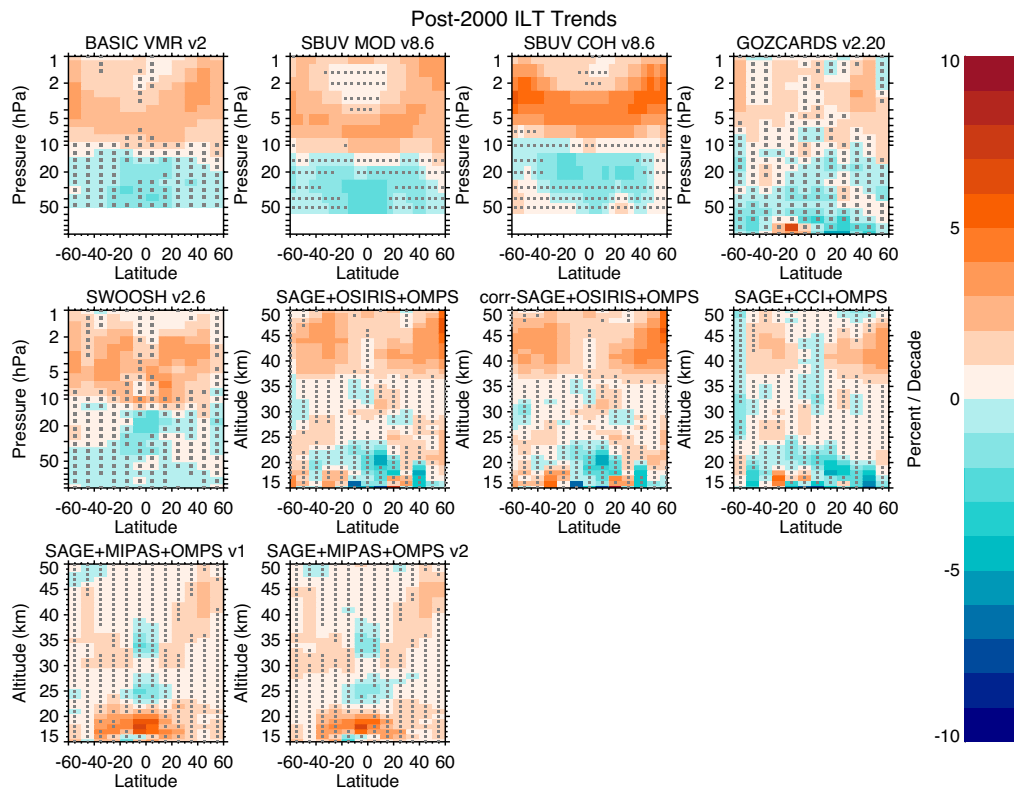


Figure S5.4: Derived trends in ozone in percent per decade for the post-2000 period (Jan 2000 – Dec 2016) for each of the satellite data sets, using the ILT trend proxy in a regression analysis. Grey stippling denotes results that are not significant at the 2-sigma level. Data are presented on their natural latitudinal grid and vertical coordinate.

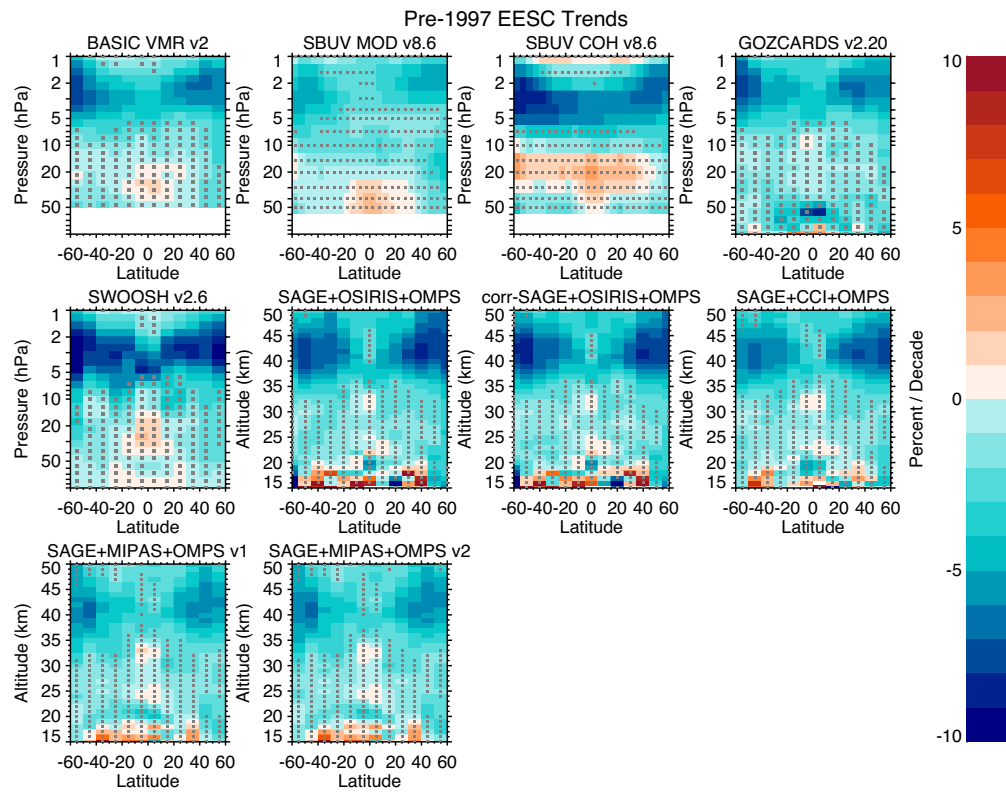


Figure S5.5: Derived trends in ozone in percent per decade for the pre-1997 period (Jan 1985 – Dec 1996) for each of the satellite data sets, using two EESC EOFs in a regression analysis. Grey stippling denotes results that are not significant at the 2-sigma level. Data are presented on their natural latitudinal grid and vertical coordinate.

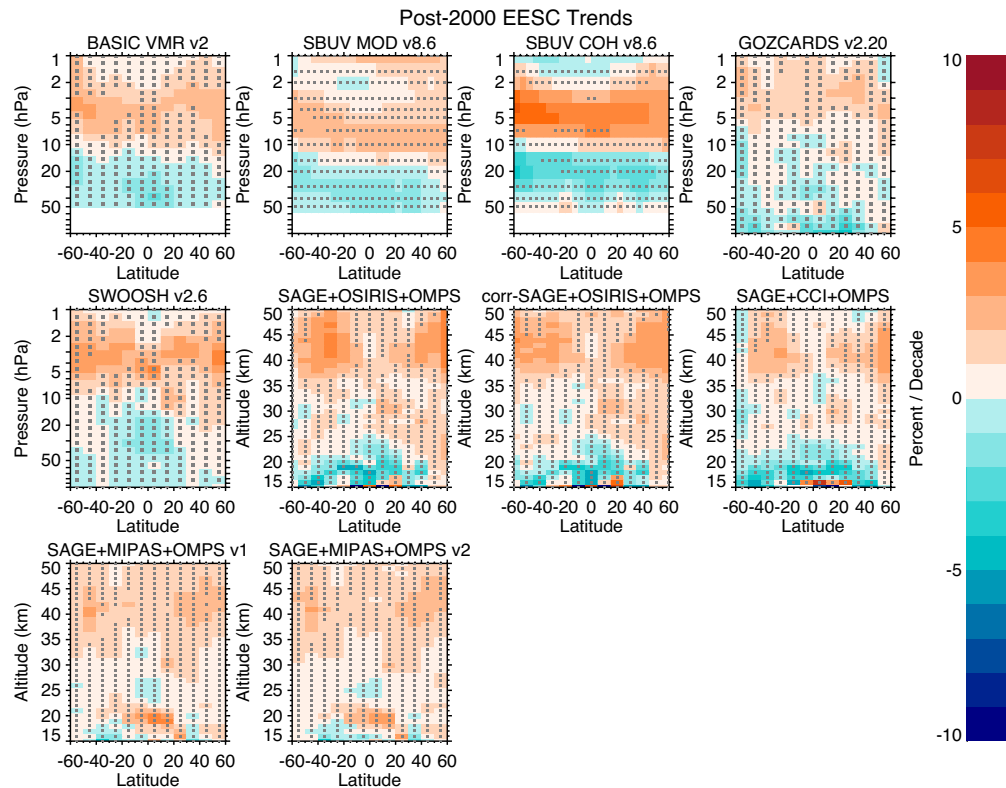


Figure S5.6: Derived trends in ozone in percent per decade for the post-2000 period (Jan 2000 – Dec 2016) for each of the satellite data sets, using two EESC EOFs in a regression analysis. Grey stippling denotes results that are not significant at the 2-sigma level. Data are presented on their natural latitudinal grid and vertical coordinate.

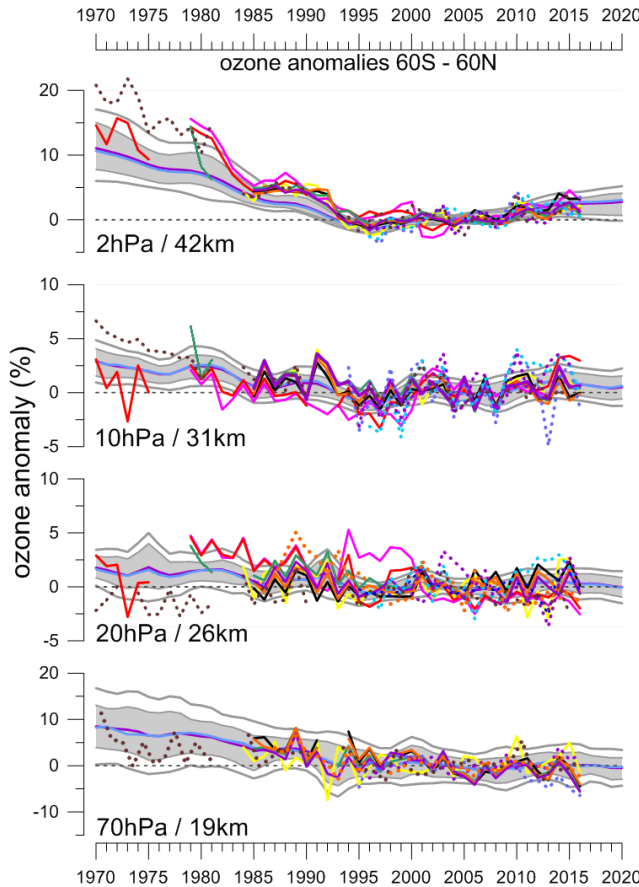


Figure S5.7: The evolution of ozone changes as annual mean anomalies at the 2 hPa/42 km, 10 hPa/31 km, 20 hPa/26 km, and 70 hPa/19 km levels for near global ozone (60°S – 60°N). Satellite data are based on zonal means, and ground-based stations are averaged over the latitude band. The grey “envelope” gives the CCM1-1 model results, based on the models 10th and 90th percentile. The model mean and the median are also plotted, together with the ± 2 standard deviation range of the models. All anomalies are calculated over the base period 1998–2008, and the CCM1-1 models are shown as 5-year weighted averages (see Chapter 5 for more details).

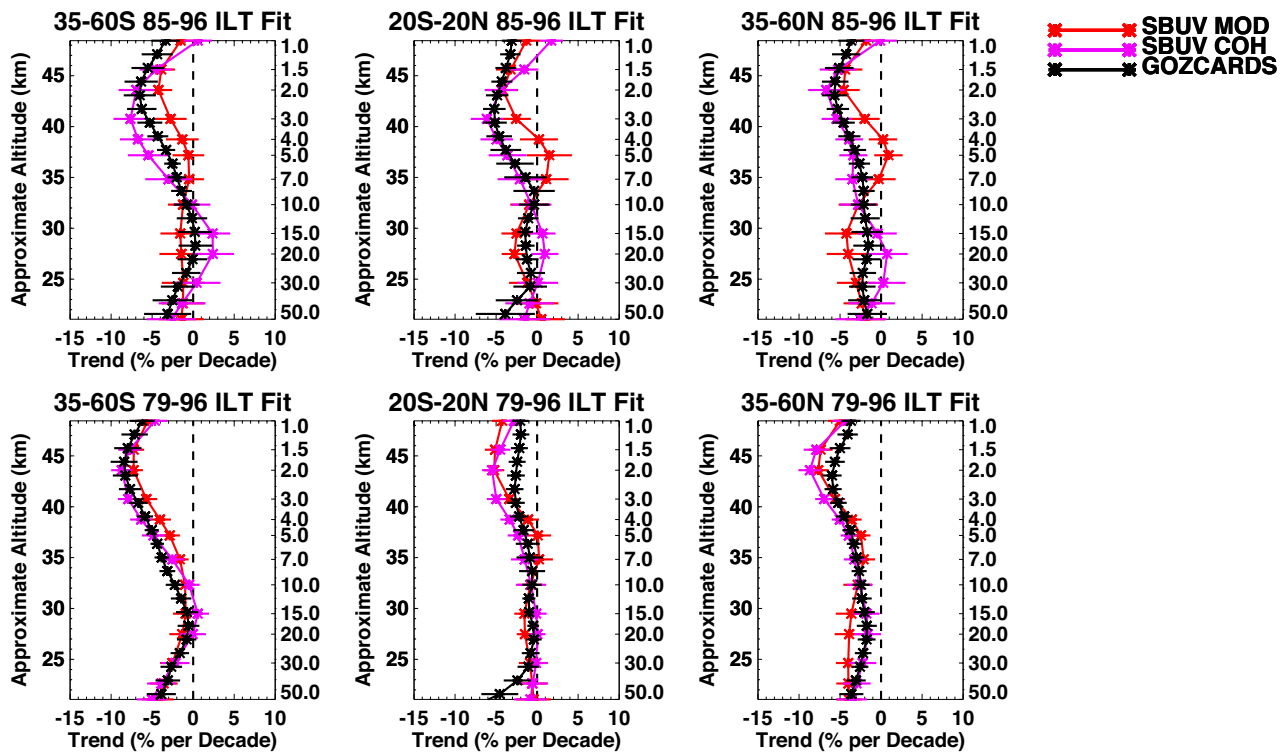


Figure S5.8: The influence of start time on pre-1997 trends (Jan 1985 – Dec 1996) derived from SBUV MOD, SBUV COH, and GOZCARDS data using the “LOTUS regression” model. Top row shows the period used for the final LOTUS analyses; bottom row shows trends that start six years earlier in time. Computing the trend over the longer time period reduces the sensitivity of the SBUV-based trend fits to the mid-1990s endpoint, a period of known problems in the SBUV individual records and thus of higher uncertainty in both merged records. Error bars denote 2-sigma uncertainty of the ILT regression fit. Pressure is denoted by the vertical scale on the right side of each panel. This Figure is discussed in detail in Section 5.1.2.

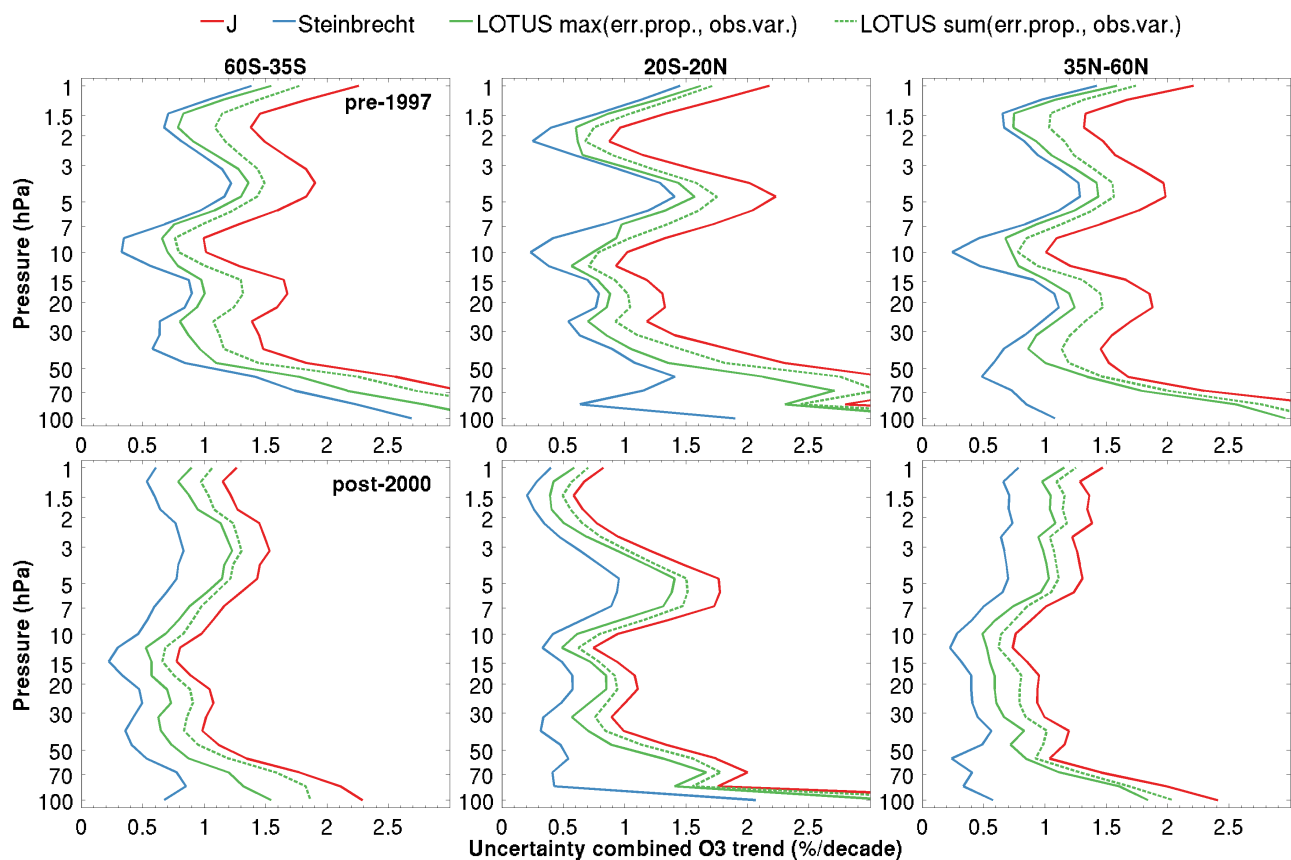


Figure S5.9: Uncertainty (1σ) of combined satellite ILT trends for pre-1997 trends (top) and for post-2000 trends (bottom row). Shown are four methods to compute uncertainty: J-distribution (Equation 5.4), Steinbrecht (Equation 5.5), LOTUS max-method (Equation 5.1) and LOTUS sum-method (Equation 5.1 but max replaced by sum). This figure is discussed in Section 5.3.4.

S.5.2 Appendix B: Analysis of correlation between fit residuals

We computed the correlation between the fit residual time series (*i.e.*, anomaly time series minus ILT regression fit) for each pair of the six merged datasets. These values can be used as estimates of the correlation between trends from the individual data records (*Section 5.3*);

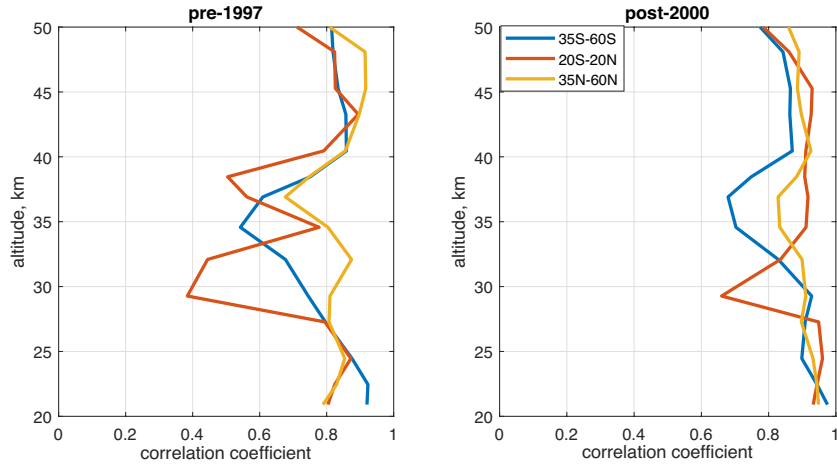


Figure S5.10: Correlation coefficients between the fit residual time series of the SBUV MOD and SBUV COH datasets, as a function of altitude, for two periods in time and three broad latitude bands.

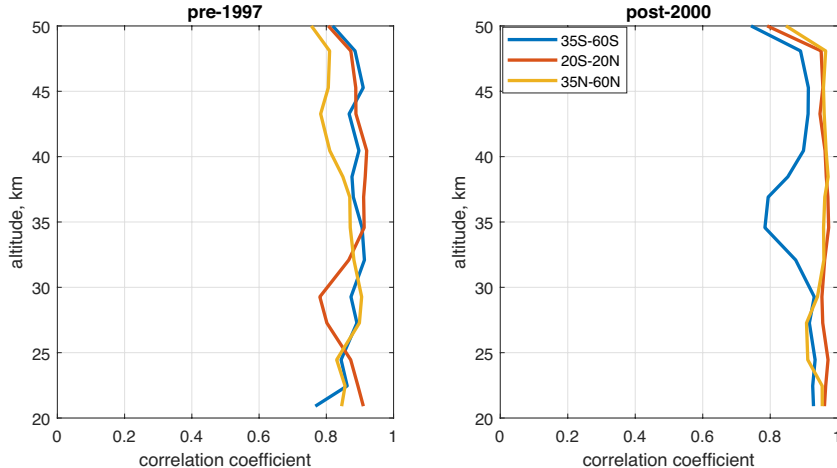


Figure S5.11: As **Figure S5.10** but for the correlation between GOZCARDS and SWOOSH.

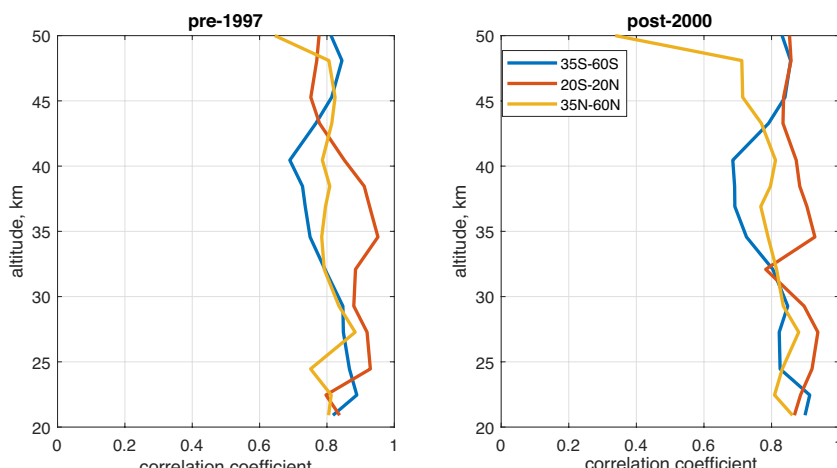


Figure S5.12: As **Figure S5.10** but for corr-SAGE-OSIRIS-OMPS and SAGE-CCI-OMPS.

presumably these represent upper limits to the unknown, true correlation. Correlations were computed separately for pre-1997 and post-2000 trends. The figures below illustrate the experimental correlation coefficients for some pairs of the datasets.

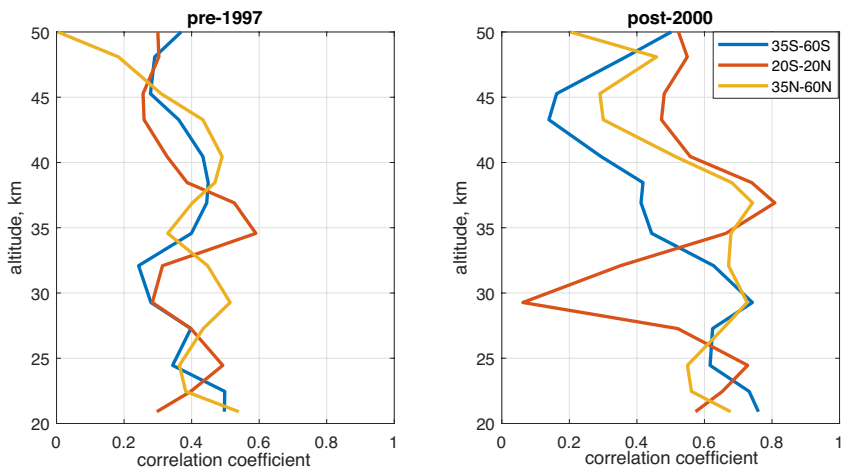


Figure S5.13: As **Figure S5.10** but for SBUV MOD and SAGE-CCI-OMPS.

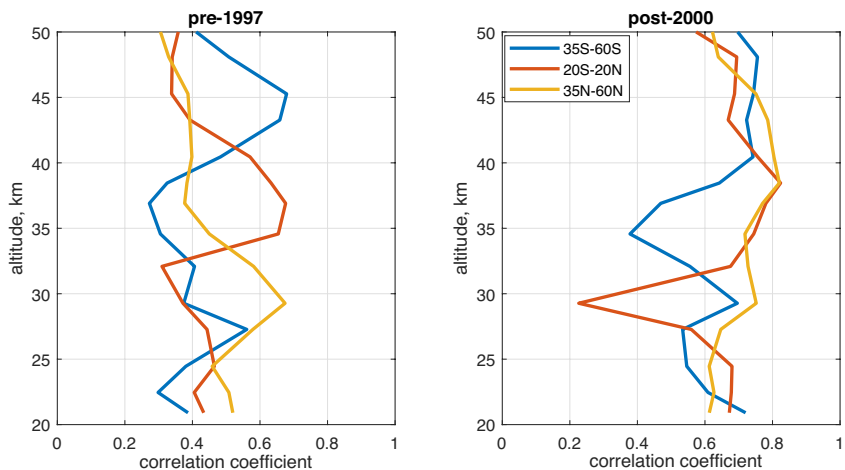


Figure S5.14: As **Figure S5.10** but for SBUV MOD and GOZCARDS.

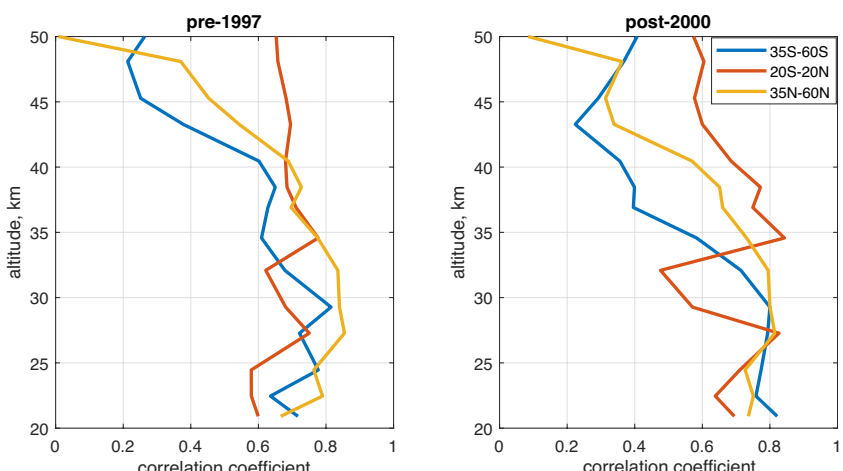


Figure S5.15: As **Figure S5.10** but for GOZCARDS and SAGE-CCI-OMPS.

S.5.3 Appendix C: Table of LOTUS trend values

Pressure (hPa)	Ozone trend Jan 1985 – Dec 1996 (% per decade, $\pm 2\sigma$)			Ozone trend Jan 2000 – Dec 2016 (% per decade, $\pm 2\sigma$)		
	60–35°S	20°S–20°N	35–60°N	60–35°S	20°S–20°N	35–60°N
1.00	-2.8 \pm 3.1	-2.0 \pm 3.2	-3.3 \pm 3.2	1.3 \pm 1.8	1.0 \pm 1.2	1.9 \pm 2.3
1.21	-3.9 \pm 2.3	-2.6 \pm 2.5	-4.2 \pm 2.2	1.8 \pm 1.6	1.0 \pm 0.8	2.4 \pm 2.0
1.47	-5.2 \pm 1.7	-3.3 \pm 1.7	-5.3 \pm 1.5	2.0 \pm 1.8	1.1 \pm 0.8	2.6 \pm 2.1
1.78	-5.9 \pm 1.6	-4.0 \pm 1.2	-5.7 \pm 1.5	2.1 \pm 1.9	1.2 \pm 0.8	2.8 \pm 2.1
2.15	-6.2 \pm 1.8	-4.6 \pm 1.2	-5.9 \pm 1.9	2.1 \pm 2.3	1.4 \pm 1.0	2.9 \pm 2.2
2.61	-5.9 \pm 2.2	-4.8 \pm 1.3	-5.3 \pm 2.1	2.3 \pm 2.4	1.5 \pm 1.4	3.1 \pm 1.9
3.16	-5.3 \pm 2.6	-4.6 \pm 2.1	-4.5 \pm 2.5	2.3 \pm 2.5	1.5 \pm 1.9	2.9 \pm 2.0
3.83	-4.5 \pm 2.7	-3.8 \pm 2.9	-3.6 \pm 2.8	2.2 \pm 2.3	1.6 \pm 2.4	2.5 \pm 2.0
4.64	-3.7 \pm 2.6	-2.9 \pm 3.1	-3.0 \pm 2.9	1.9 \pm 2.3	1.4 \pm 2.8	2.0 \pm 2.1
5.62	-2.9 \pm 2.2	-2.0 \pm 2.7	-2.6 \pm 2.5	1.6 \pm 2.0	1.3 \pm 2.8	1.5 \pm 1.9
6.81	-2.2 \pm 1.5	-1.2 \pm 2.0	-2.5 \pm 1.9	1.1 \pm 1.8	1.2 \pm 2.6	1.2 \pm 1.5
8.25	-1.6 \pm 1.3	-0.7 \pm 1.9	-2.4 \pm 1.4	0.7 \pm 1.6	1.1 \pm 1.9	0.9 \pm 1.2
10.00	-1.0 \pm 1.4	-0.8 \pm 1.5	-2.5 \pm 1.5	0.2 \pm 1.4	1.1 \pm 1.2	0.8 \pm 1.0
12.12	-0.5 \pm 1.6	-1.1 \pm 1.1	-2.2 \pm 1.6	0.0 \pm 1.1	0.6 \pm 1.0	0.7 \pm 1.1
14.68	-0.0 \pm 2.0	-1.2 \pm 1.6	-1.9 \pm 2.0	-0.0 \pm 1.1	-0.2 \pm 1.4	0.4 \pm 1.1
17.78	0.1 \pm 2.0	-1.0 \pm 1.8	-1.6 \pm 2.4	0.1 \pm 1.1	-0.4 \pm 1.7	0.0 \pm 1.2
21.54	-0.0 \pm 1.9	-0.8 \pm 1.7	-1.7 \pm 2.5	0.3 \pm 1.4	-0.5 \pm 1.7	-0.1 \pm 1.2
26.10	-0.4 \pm 1.6	-0.5 \pm 1.4	-1.9 \pm 2.2	0.4 \pm 1.5	-0.7 \pm 1.4	-0.1 \pm 1.2
31.62	-1.2 \pm 1.7	-0.9 \pm 1.7	-1.9 \pm 1.9	0.3 \pm 1.3	-1.1 \pm 1.1	-0.2 \pm 1.3
38.31	-1.7 \pm 1.9	-1.6 \pm 2.1	-1.8 \pm 1.7	0.1 \pm 1.3	-1.4 \pm 1.4	0.1 \pm 1.7
46.42	-2.1 \pm 2.2	-1.9 \pm 2.7	-1.8 \pm 2.0	-0.2 \pm 1.5	-1.0 \pm 1.8	0.3 \pm 1.4
56.23	-2.2 \pm 3.5	-3.3 \pm 4.3	-2.4 \pm 2.7	-0.6 \pm 1.8	-0.6 \pm 2.6	0.1 \pm 1.7
68.13	-1.5 \pm 4.3	-1.9 \pm 5.4	-4.2 \pm 3.6	-0.5 \pm 2.4	-0.9 \pm 3.3	-0.7 \pm 2.2
82.54	0.0 \pm 5.6	-1.7 \pm 4.6	-6.1 \pm 5.1	-0.7 \pm 2.6	0.2 \pm 2.8	-1.8 \pm 3.2
100.00	3.2 \pm 6.7	-3.0 \pm 7.4	-7.5 \pm 5.9	-0.1 \pm 3.1	-4.2 \pm 6.4	-2.2 \pm 3.7

Table S5.1: Overview of LOTUS combined satellite trends in three latitude bands and two time periods, for the 25 pressure levels used in the analysis. Central values and uncertainties represent the 95 % confidence interval. Trend results that are statistically significant at the 2-sigma level are highlighted in grey cells. Trend results from six merged satellite records are combined here: GOZCARDS v2.20, SWOOSH v2.6, SBUV MOD v8.6, SBUV COH v8.6, SAGE-OSIRIS-OMPS, and SAGE-CCI-OMPS. See also **Figures 5.12 and 5.14**.

